Weyl fermion excitations in the ideal Weyl semimetal $CuTlSe_2$

C. N. Wang [1,*] D. Tay [2,*] Q. X. Dong,[3,*] Z. Okvátovity,[4,5] B. M. Huddart [6] C. Y. Ma,[3] K. Yokoyama [7] L. Yu,[3] T. Lancaster [6] G. F. Chen,[3,†] H.-R. Ott,[2] and T. Shiroka [2,8,‡]

[1]*Department of Physics, University of Fribourg, CH-1700 Fribourg, Switzerland*
[2]*Laboratorium für Festkörperphysik, ETH Zürich, CH-8093 Zurich, Switzerland*
[3]*Beijing National Laboratory for Condensed Matter Physics and Institute of Physics, Chinese Academy of Sciences, Beijing 100190, People's Republic of China*
[4]*Department of Theoretical Physics, Budapest University of Technology and Economics, 1521 Budapest, Hungary*
[5]*MTA-BME Lendület Topology and Correlation Research Group, Budapest University of Technology and Economics, 1521 Budapest, Hungary*
[6]*Department of Physics, Centre for Materials Physics, Durham University, South Road, Durham DH1 3LE, United Kingdom*
[7]*ISIS Pulsed Neutron and Muon Source, Rutherford Appleton Laboratory, Chilton, Didcot OX11 0QX, United Kingdom*
[8]*Laboratory for Muon Spin Spectroscopy, Paul Scherrer Institut, CH-5232 Villigen PSI, Switzerland*

(Received 4 April 2024; accepted 7 August 2024; published 3 September 2024)

An ideal Weyl semimetal is characterized by a dispersion in which only Weyl cones intersect the Fermi level, with low-energy behavior being governed by Weyl fermions. Although ideal Weyl semimetals have long been anticipated, only a few are realized in nonmagnetic materials. In this study, we confirm the presence of Weyl-fermion excitations in the ideal Weyl semimetal $CuTlSe_2$ via a combination of magnetoresistance, Hall-effect, magnetic-susceptibility, nuclear magnetic resonance (NMR), and muon-spin relaxation (μSR) experiments. Magnetoresistance measurements reveal a negative longitudinal magnetoresistance (LMR), which scales as B^2, while Hall-effect results indicate a predominant contribution from Weyl fermions with a hole-type charge. Magnetic susceptibility and μSR measurements indicate the lack of any intrinsic spontaneous magnetic moments down to base temperature. Finally, the NMR results can be modeled by a two-component effective Hamiltonian, which reproduces well the temperature-dependent ^{63}Cu NMR $(T_1T)^{-1}$ factor, shown to scale as T^2 below 100 K and as T^1 above 100 K. Overall, we find that the extremely low concentration (10^{17} cm^{-3}) of carriers in $CuTlSe_2$ originates from an ideal nonmagnetic Weyl semimetallic state, persisting up to a thermal excitation energy of 9 meV (100 K), above which trivial electronic bands close to E_F take over. Our findings highlight $CuTlSe_2$ as a new member of the intriguing class of Weyl semimetals.

DOI: 10.1103/PhysRevResearch.6.033229

I. INTRODUCTION

Weyl semimetals continue to attract research interest both theoretically and experimentally [1]. These materials host massless Weyl fermions, which are defined by pairs of linearly dispersing, nondegenerate spin-polarized conduction and valence bands intersecting at isolated locations (Weyl points) in momentum space [2]. The corresponding quasiparticles, constituting the state's low-energy excitations, have the properties of Weyl fermions, as described by the Weyl equation [3,4]. Their transport properties reflect these low-energy excitations. For instance, as a result of the chiral anomaly, negative longitudinal magnetoresistance (LMR) is a means of identifying a Weyl semimetal [5].

Materials breaking the time-reversal symmetry (TRS) are favorable to hosting Weyl fermions [6]. In this case, magnetism plays a key role in determining the topological behavior of electronic states, either by protecting them or by stabilizing the topological bands. It is not uncommon for magnetism to be one of the characteristic emergent properties that distinguish between different topological materials, as recently predicted for a large number of compounds [7]. The presence of a spontaneous magnetic field can be confirmed through the use of local magnetic probes, such as nuclear magnetic resonance (NMR) and muon-spin relaxation (μSR). Lately, NMR has demonstrated a growing potential as a sensitive probe for studying the Weyl-fermion excitations [8–12]. This is due to its energy resolution of the order of microelectronvolts (μeV) which, not only matches well that of electronic excitations, but is also three orders of magnitude better than that typically encountered in other electronic probes.

Theoretical investigations indicate that numerous compounds have the potential for hosting Weyl nodes [13]. However, these compounds are frequently accompanied by trivial electronic bands that also intersect the Fermi level. A subset of Weyl materials, ideal Weyl semimetals, are specific types of semimetals where the trivial electronic bands are away from the Fermi level, thus resulting uniquely in a Weyl semimetal phase. Compounds that exhibit characteristics of ideal Weyl semimetals are still quite scarce, with only a handful having been confirmed so far, as, e.g., $MnBi_2Te_4$ [14],

*These authors contributed equally to this work.
†Contact author: gfchen@iphy.ac.cn
‡Contact author: tshiroka@phys.ethz.ch

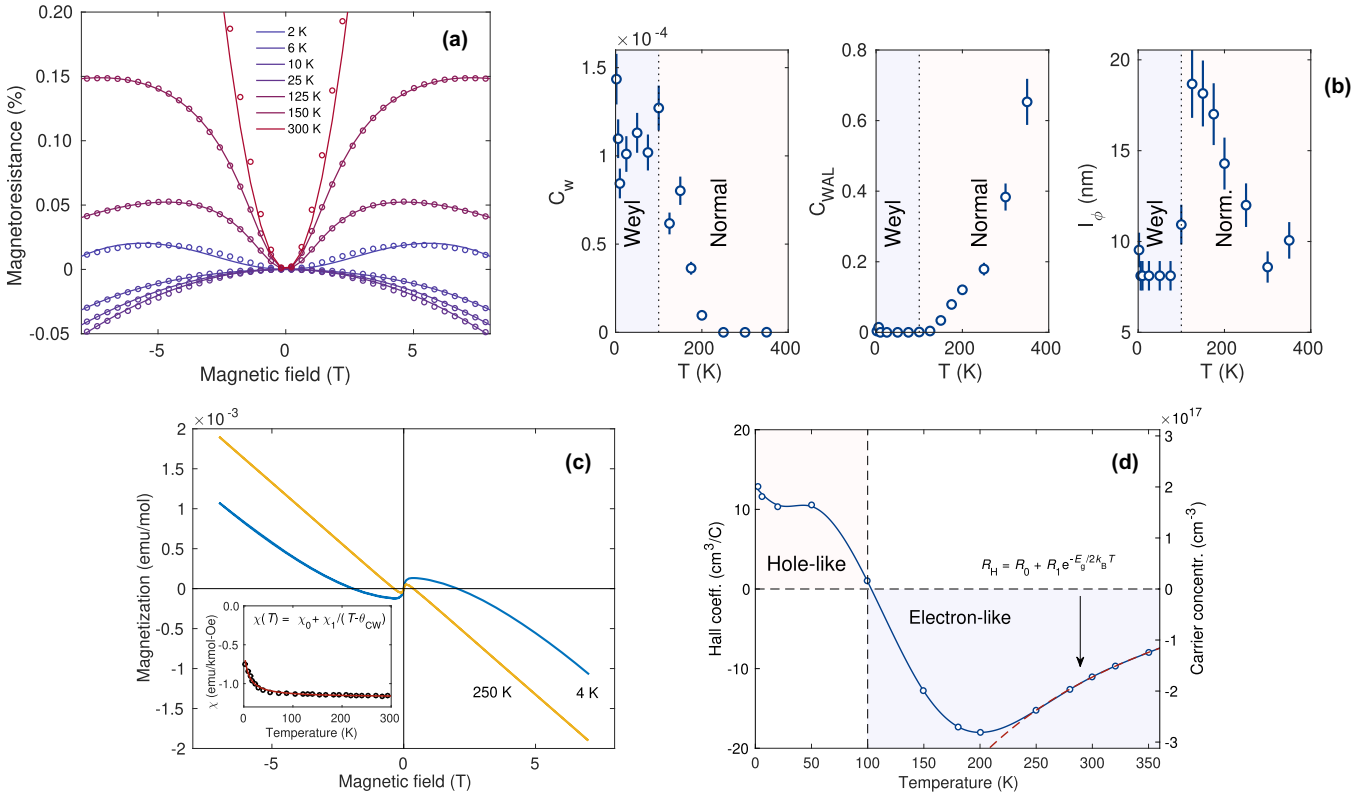

FIG. 1. Magnetoresistance and magnetic susceptibility of $CuTlSe_2$. (a) Temperature-dependent magnetoresistance curves of $CuTlSe_2$ measured at an angle of zero degrees. The negative-curvature low-T data are typical of Weyl fermion systems. (b) Fit parameters of magnetoresistance vs temperature illustrate clearly two different regimes across 100 K, here shown in different colors. (c) Field- and temperature-dependent magnetic susceptibility. (main): M vs H curve at 4 K and 250 K, showing diamagnetic behavior and a slight magnetic impurity. (Inset) Temperature dependence of magnetic susceptibility at $B = 5$ T. (d) Temperature-dependent Hall coefficient. Similar to panel (b), close to 100 K there is a change in the character of carriers: from electronlike above 100 K, to holelike below it.

which shows time-reversal symmetry breaking (TRSB) [2]. In this study, we present $CuTlSe_2$, an ideal Weyl semimetal candidate, which preserves TRS [15]. $CuTlSe_2$ belongs to the chalcopyrite family, crystallizing in a body-centered tetragonal structure with space group $I\bar{4}2d$ (No. 122). Density functional theory (DFT) calculations predict that only a single linearly dispersed band crosses E_F [15]. Our systematic investigation of the magnetic properties of $CuTlSe_2$, utilizing both bulk-probe techniques (magnetometry and Hall-effect measurements), as well as local-probe methods (NMR and μSR), provide a comprehensive understanding of the magnetic properties of $CuTlSe_2$, along with the confirmation of the existence of Weyl-fermion excitations in this compound.

II. NEGATIVE MAGNETORESISTANCE IN $CuTlSe_2$

A common signature of Weyl fermions is the Adler-Bell-Jackiw chiral anomaly [5,16]. This occurs when a single Weyl fermion couples to an electromagnetic field with $\boldsymbol{B} \parallel \boldsymbol{E}$ and results in the nonconservation of electric charge [17]. The chiral anomaly can be measured via nonlocal transport measurements [18] or via classical magnetoresistance measurements, for which theory predicts a negative longitudinal magnetoresistance (LMR) that scales as B^2 [19].

Experimentally, a negative LMR has been reported in many Weyl semimetals, such as TaAs [20,21], TaP [22], and NbP [23]. However, the magnitude of the observed negative magnetoresistance varies widely: from ∼2% in TaP, to ∼10% in NbP, to ∼30% in TaAs. Furthermore, in all these systems, the negative LMR for $\boldsymbol{B} \parallel \boldsymbol{E}$ is accompanied by a large positive magnetoresistance at other angles. The latter reflects the electron-hole resonance, which occurs in semimetals whose conduction is due to both electrons and holes [24]. LMR data for $CuTlSe_2$ and their fits at selected temperatures are shown in Fig. 1(a). Our observations differ from those of the above systems in several respects.

First, the negative magnetoresistance observed in $CuTlSe_2$ is of rather modest magnitude. To model the negative magnetoresistance, we fit the curves of MR versus B using the theoretical formulation of Zhang *et al.* [21]. Details of this model can be found in the Appendix. In this case, the magnetoresistance is given as the sum of a chiral anomaly term proportional to C_W, which reflects the Weyl physics, and a weak Anderson localization (WAL) term proportional to C_{WAL}, which arises from the disorder-induced scattering. The temperature evolution of the fit parameters C_W, C_{WAL}, and the coherence length l_ϕ is reported in Fig. 1(b). At room temperature, the C_{WAL} term dominates, a feature which can be explained by the short coherence length l_ϕ, here found to be of the order of 10 nm. However, as the temperature is lowered, l_ϕ increases and the coherence term C_{WAL} decreases, while the chiral transport term C_W starts to increase. Below 10 K

and above the crossover field ($B_c \approx 3$ T), the magnetoresistance turns negative (note the downward arms in Fig. 1(a) for $|B| > 3$ T), indicating that the chiral transport term dominates.

Second, unlike in TaAs, TaP, or NbP, we do not observe any electron-hole resonance below 100 K. To understand the lack of such a feature, we calculate the charge-carrier density in $CuTlSe_2$, as obtained from the Hall-effect measurements. The results of this calculation are shown in Fig. 1(d), where the electron densities are of the order of 10^{17} cm^{-3}, i.e., 100 times lower than in TaP [22]. Hence, the weak negative LMR of $CuTlSe_2$ can be ascribed to its low carrier density. We end this section by noting that systems unrelated to Weyl fermions can also possess negative LMR (see, e.g., Ref. [25]), so other measurements including NMR and μSR are needed to confirm the Weyl fermion excitations in $CuTlSe_2$.

III. MACROSCOPIC MAGNETIC RESPONSE OF $CuTlSe_2$

The temperature dependence of magnetic susceptibility for single crystals of $CuTlSe_2$ in an external magnetic field of 5 T with $H \parallel c$ is given in the inset of Fig. 1(c). The total susceptibility can be fitted with

$$\chi(T) = \chi_0 + \chi_1/(T - \Theta_W). \quad (1)$$

Here, χ_0 describes a temperature-independent term, while the $\chi_1/(T - \Theta_W)$ term describes the magnetic component. Equation (1) provides two key insights. First, we note that the temperature term χ_0 in $CuTlSe_2$ is negative, indicating a diamagnetic response, in accordance with the theoretical prediction for Weyl semimetals [26,27]. Second, we note that the temperature-dependent susceptibility does not follow the $\log(T)$ dependence predicted for Weyl semimetals [26,27], but instead it follows a Curie-Weiss law with $\theta_W = 0.25$ K. This indicates an unexpected magnetic behavior (albeit with a tiny θ_W) of either intrinsic or extrinsic origin.

First, we discuss the possibility of intrinsic magnetism. According to theory, in $CuTlSe_2$, the spatial-inversion symmetry is broken on account of its tetragonal distortion and the ensuing atom displacements [15]. Indeed, x-ray diffraction measurements conducted at 100 and 295 K (details in Appendix) confirm that the compound possesses a noncentrosymmetric structure with point group $I\bar{4}2d$. Hence, time-reversal symmetry breaking is not strictly required to realize the Weyl points. Nonetheless, since Cu has two oxidation states [Cu(I) and Cu(II)], with either 0 or 1 unpaired electrons, it is possible that the presence of Cu impurities may modify the magnetic properties of the majority phase, leading to TRS breaking and/or other intrinsic magnetic effects in the bulk.

Next, we consider the alternative hypothesis, namely that the observed susceptibility behavior is due to extrinsic contaminants in our sample. Note that, since the intrinsic diamagnetism of $CuTlSe_2$ is relatively small, even tiny traces of paramagnetic contaminants can have disproportionate effects on the magnetic susceptibility. Conversely, as we show below, in all the other local-probe measurements, the effect of impurities, if any, is negligible. We note that, in $CuTlSe_2$, Cu has an oxidation state of +1 (with zero unpaired electrons). Considering that Cu(I) is diamagnetic, whereas Cu(II) is paramagnetic, it is very likely that possible magnetic contaminants consist of some compound of Cu(II).

To confirm whether the $\chi_1/(T - \Theta_W)$ term is due to Cu (II) contaminants or is intrinsic to $CuTlSe_2$, we investigated the magnetic properties of $CuTlSe_2$ by utilizing local-probe techniques, such as NMR and μSR. As we show in the next section, the combination of both techniques allows us to conclude that the upturn in Fig. 1(c) arises from a minority of extrinsic magnetic contaminants and not from the majority intrinsic phase.

IV. LACK OF INTRINSIC MAGNETIC MOMENTS OF ELECTRONIC ORIGIN

Although macroscopic measurements suggest traces of paramagnetism at low temperatures, we demonstrate that this is not an intrinsic property of $CuTlSe_2$, but rather arises from a minority phase or impurities.

To investigate the magnetic properties of $CuTlSe_2$, we employed the μSR technique, well known for its high sensitivity to local magnetic fields [28]. As shown in Fig. 2(a), upon zero-field (ZF) cooling, the muon-spin depolarization does not change significantly between 1.5 and 100 K, while larger changes are clearly seen above 180 K. The ZF-μSR spectra can be phenomenologically described with a two-component muon-depolarization function, as detailed in the Appendix. The majority of muon spins depolarize following a Gaussian decay with a depolarization rate $\sigma = 0.15(1)$ MHz. At short times (earlier than 0.01 μs), we observe also a rapid decay of the muon depolarization. On the time scale of Fig. 2(a), this appears as a reduction of the initial muon asymmetry (compared to its typical value of ca. 0.25). A rapid decay of muon depolarization is normally attributed to the presence of strong and broadly distributed local magnetic fields at the muon site, here, most likely associated to paramagnetic impurities. Measurements in a weak transverse magnetic field, shown in Fig. 2(b), allow us to evaluate the corresponding volume fraction of this minority phase as 6(1)%. This value provides an upper boundary for the magnetic impurity volume, since other factors (such as the formation of muonium) may contribute to the missing initial asymmetry.

At the same time, the depolarization rate at the base temperature of the majority phase is quite small, $\sigma = 0.15(1)$ MHz. Nevertheless, this may still be ascribed to the contribution of electronic magnetic moments [29]. To check this assumption, we estimated the dipolar field strength at the muon site by taking into account the contributions from the surrounding nuclear moments. As illustrated in Figs. 2(c) and 2(d), our calculations suggest that there are two classes of muon sites: low-energy sites, where the muon sits on the edge of the cell, 1.5 Å from a Se atom, and secondary sites, where the muon sits between a Cu and a Se atom, 1.5 Å apart from the latter. These two classes are close in energy, with the second one lying ∼0.15 eV higher. In both cases, the proximity of muon to Se is reminiscent of the affinity of muons for oxygen (similar in electronegativity to Se and belonging to group 16). To reconcile the muon-stopping sites with the measured spectra, we computed the expected muon-relaxation rate by using the van Vleck second moment [28]. We obtain a relaxation rate $\sigma = 0.13(4)$ MHz (under the same convention used in the fitting function) for the first class of

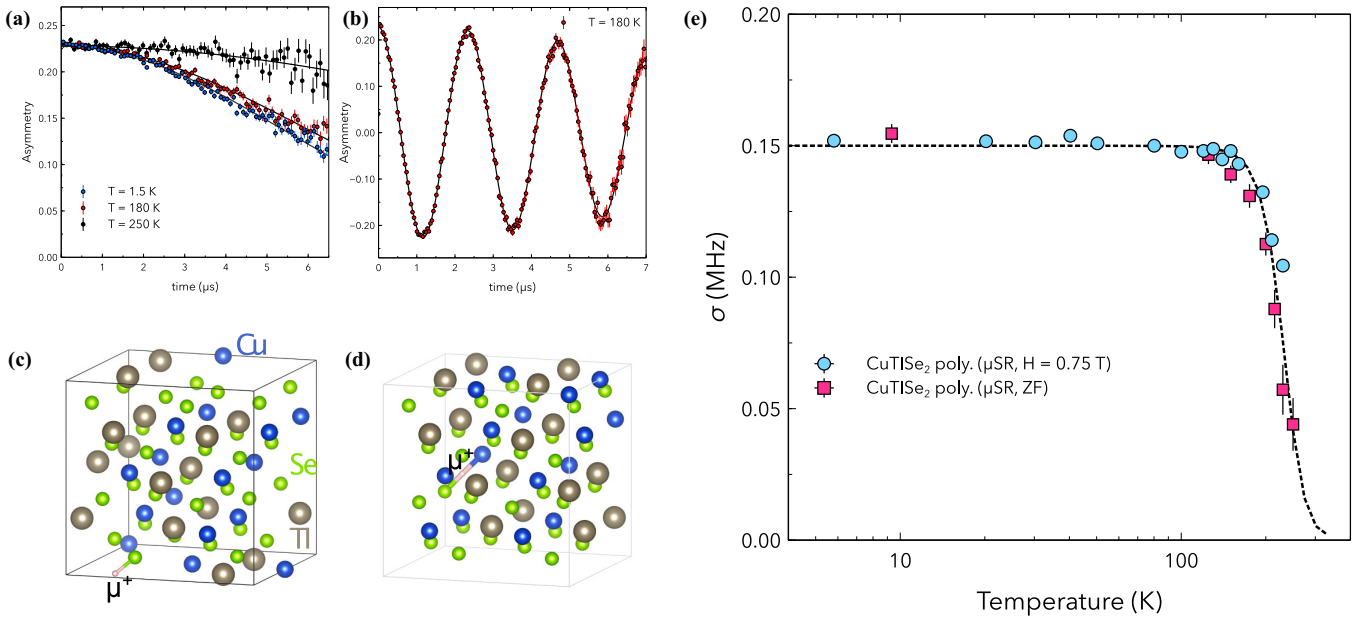

FIG. 2. (a) Zero-field μSR data recorded at 1.5 and 180 K. Time spectra were analyzed with a Gaussian depolarization function, as described in the text. The instrumental asymmetry was determined to be 0.245. (b) Transverse-field μSR data measured at 180 K in an applied magnetic field of 3 mT. (c), (d) Schematic illustration of the two types of muon-stopping sites in $CuTlSe_2$. (e) Gaussian depolarization rates vs temperature, measured at different magnetic fields: zero-field and 0.75 T transverse field.

sites and 0.24(4) MHz for the second. Based on this result, we conclude that the observed muon-spin depolarization is primarily due to the nuclear dipolar fields. Even by assuming that a part of the observed muon-spin depolarization is associated with electronic magnetic moments, its magnitude would be significantly less than 0.15(1) MHz. Overall, our μSR results indicate the absence of dynamic- or static magnetic moments of electronic origin. Further, at base temperature, muons are located predominantly at the second site, where the surrounding nuclei contribute to the muon-spin depolarization via dipolar interactions.

In the considered temperature range below room temperature, the nuclear magnetic moments exhibit quasistatic behavior and maintain constant amplitude. Since the muon depolarization rate is almost exclusively due to them, we expect an essentially temperature-independent muon-spin depolarization. In Fig. 2(e), instead, σ exhibits a strong temperature dependence common to both the zero-field (ZF) and the 0.75 T transverse-field (TF) cases. This outcome reveals a consistent field-independent behavior. Below T_{onset} of about 150 K, σ remains constant [at circa 0.15(1) MHz], while, above T_{onset}, the depolarization rate decreases monotonically to less than 0.01 MHz at 300 K. Since the rate of depolarization is independent of the strength and direction of the applied magnetic field (the independence of the direction is deduced from measurements on single crystals), this implies that the depolarization is dominated by the isotropic contribution of the hyperfine coupling of nuclei with muons. The general temperature-dependent trend of σ is phenomenologically described by a sigmoid function, typical of a temperature-activated crossover behavior:

$$A(T) = \frac{A_i - A_f}{1 + e^{(T-T_c)/\Delta T}} + A_f, \tag{2}$$

where T_c is the midvalue between the initial- and final states, A_i and A_f, while ΔT is the slope factor. As mentioned above, muon-site calculations set a lower boundary of about 0.13(4) MHz for the nuclear depolarization rate in $CuTlSe_2$. Consequently, the observed overall decrease of σ cannot be simply assigned to a static muon redistribution among magnetically inequivalent sites at elevated temperatures, but it may also be accompanied by motional narrowing effects (due to repeated muon release- and trapping processes [30]), so that muons become sensitive to the reconstruction of the electronic cloud around them via a diffusive mechanism [31]. Notably, it has also been reported that quasiparticle scattering can modulate the muon hyperfine coupling, thus allowing muons to become sensitive to the electronic state and provide insight, albeit indirectly, into the electronic transitions [32]. Note that, we still cannot exclude other mechanisms of a continuous transition of the electronic states close to the Fermi energy (with a broad onset around 150 K), whose details depend on the subtleties of the free-energy profile.

V. ANOMALOUS HYPERFINE COUPLING IN $CuTlSe_2$

It has been demonstrated that Weyl fermions can give rise to an anomalous hyperfine coupling with the nuclear magnetic moments [33]. Such coupling can be detected by NMR, via two distinct signatures, namely in the temperature dependence of NMR shifts and of relaxation rates.

NMR shifts are expected to follow a $\log(T)$ dependence with temperature [27]. The experimentally determined NMR lineshape for the ^{63,65}Cu nuclei are plotted in Fig. 3(a). As can be seen, the lineshapes exhibit a Gaussian profile, typical of powdered samples which average out most of the angle-dependent anisotropies. Further, we note that neither the lineshapes, nor the relaxation rates show a field dependence.

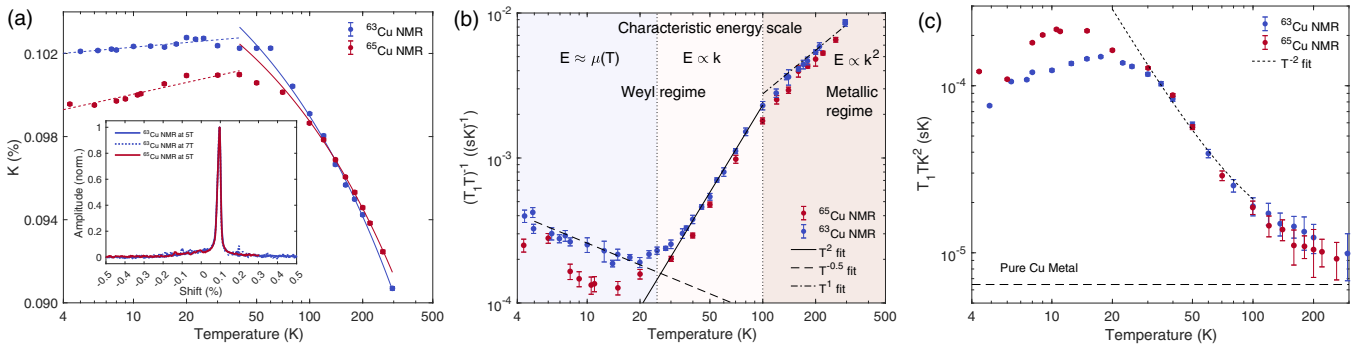

FIG. 3. NMR shifts and relaxations evidence a Weyl-semimetal behavior in $CuTlSe_2$. (a) Temperature dependence of the ^{63,65}Cu NMR shifts. Dashed lines are fits to the logarithmic function $K = a + b\log(T)$ (in the Weyl regime), while solid lines are fits to the power law $K = a - b\sqrt{T}$. Inset: ^{63,65}Cu NMR line shapes are independent of the magnetic field and probe nucleus. (b) Temperature dependence of the ^{63,65}Cu spin-lattice relaxation rates. Three regions with different scaling behaviors are highlighted. (c) Temperature dependence of the Korringa product of ^{63,65}Cu. Isotope-dependent differences in K and T_1 cancel out, making the Korringa product almost the same.

Hence, in our analysis, the 5 and 7 T datasets were combined together. Upon inspecting the experimental results shown in Fig. 3(a), we observe that the NMR shifts versus temperature indeed follow a logarithmic law up to about 50 K, smeared out by a Fermi-liquid regime at higher T.

Theory also predicts that the NMR relaxation rates should follow a power-law dependence with temperature [27]. Indeed, in Fig. 3(b), we observe that, up to 100 K, $CuTlSe_2$ follows a $(T_1T)^{-1} \propto T^2$ dependence, as proposed for an ideal Weyl semimetal.

In addition, at temperatures below 20 K, $(T_1T)^{-1}$ decreases with temperature as $\sim T^{-0.5}$. A -0.5 exponent is also observed in the ^{181}Ta NQR relaxation of TaP and TaAs single crystals [8,9]. These results suggest that a power-law dependence with a negative coefficient may be a common feature of Weyl semimetals at low temperatures.

There are two competing theories regarding the low-temperature behavior of Weyl semimetals. The original paper by Yasuoka *et al.* [8] uses a phenomenological two-channel relaxation, where one of the channels, independent of the Weyl point, is responsible for the initial decrease of $1/(T_1T)$ with temperature, whereas the other channel follows an activated Weyl-type behavior, $\sim T^2 \exp(-\Delta/k_BT)$, responsible for the expected T^2 scaling. In a subsequent model by Okvátovity *et al.* [27], described in more detail in the next section, the crossover in $1/(T_1T)$ is explained without the need for a new relaxation channel, simply by invoking a temperature-dependent chemical potential $\mu(T)$.

In this picture, the chemical potential μ exhibits an initial decrease identical to that of the normal Fermi gas, with a typical energy scale of 10^4 K. However, in Weyl semimetals, this energy scale drops to the 10–100 K region [27], which eventually allows us to observe the crossover in $1/(T_1T)$ behavior: from Weyl-like below 100 K, to normal above it [regions $E \approx \mu(T)$ and $E \propto k$ versus $E \propto k^2$ in Fig. 3(b)]. To distinguish between the two models, we compare the isotope-dependent NMR parameters. In the case of the ^{63}Cu and ^{65}Cu isotopes, the chemical potential theory [see Eq. (7) below] predicts that the NMR relaxation rates should scale as the square of the gyromagnetic ratios, but the shape of the $(T_1T)^{-1}$ versus T curve should remain the same. Indeed, in Fig. 3, we observe that ^{63}Cu and ^{65}Cu nuclei show a very similar $(T_1T)^{-1}$ versus T behavior, except at low-T (below 20 K).

Since ^{63}Cu and ^{65}Cu are both quadrupolar nuclei, yet with different quadrupole- Q and gyromagnetic γ values, it is possible that this difference is due to the interplay between the quadrupolar and magnetic relaxation. To check this hypothesis, in Fig. 4, we plot the ratio of the ^{65}Cu and ^{63}Cu NMR relaxation rates, which turns out to be weakly temperature dependent. However, below 20 K, the ratio of the NMR relaxation rates is lower than the ratio of either the γ or Q factors. This puzzling result suggest that at low T other mechanisms, common to Weyl semimetals but yet to be clarified, are at play.

Finally, we note that, above 100 K, the NMR shift scales as $\sqrt{T}$, while $(T_1T)^{-1}$ scales as T [see Figs. 3(a) and 3(b)]. In this regime, the Korringa product T_1TK^2 approaches a constant value, not far from that of metallic Cu [see Fig. 3(c)]. Such transition to a typical Fermi-liquid behavior is confirmed also by the Hall coefficient [see Fig. 1(a)] which, above 100 K,

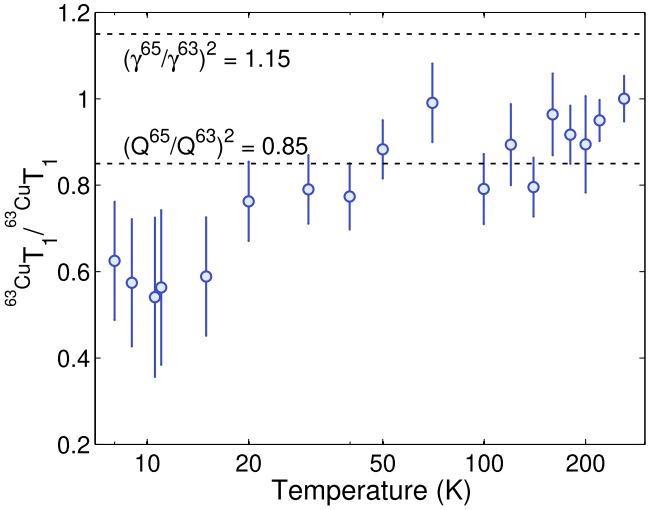

FIG. 4. Dipolar vs quadrupole relaxation rates. Ratio of dipolar and quadrupole relaxation rates for ^{63}Cu and ^{65}Cu NMR. The horizontal dashed lines refer to the theoretical values.

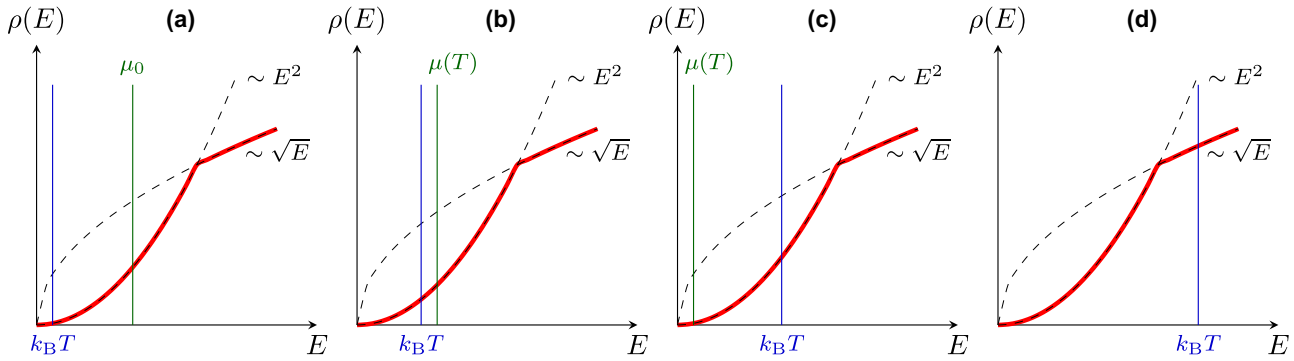

FIG. 5. Theory model accounting for Weyl physics. The dispersion relation of a typical Weyl system is linear in momentum, i.e., $E \propto k$ leading to a density of states $\rho(E) \propto E^2$. With the addition of a quadratic term to the Hamiltonian, the dispersion relation obtains an $E \propto k^2$ contribution with a corresponding DOS $\rho(E) \propto \sqrt{E}$. The transition from the Weyl regime to the normal metallic regime, where the quadratic term of the Hamiltonian is dominant induces a transition in the DOS from $\propto E^2$ to $\propto \sqrt{E}$, which is observable in the relaxation rate.

follows a $R_{\mathrm{H}} \propto \exp(-E_0/2k_{\mathrm{B}}T)$ dependence, indicative of thermally activated charge carriers.

VI. TWO-COMPONENT EFFECTIVE HAMILTONIAN

To explain qualitatively the behavior of $CuTlSe_2$ across the entire temperature range, we introduce a low-energy effective Hamiltonian by adding a quadratic term to the original Weyl Hamiltonian [27]:

$$\mathscr{H} = \frac{\hbar^2 k^2}{2m^*}\sigma_0 + \hbar v_{\mathrm{F}}(k_x\sigma_x + k_y\sigma_y + k_z\sigma_z). \tag{3}$$

Here, $\sigma_x, \sigma_y, \sigma_z$ are the Pauli matrices, σ_0 is the identity matrix, v_{F} is the Fermi velocity, and m^* is the effective mass. Equation (3) is based on the effective Hamiltonian obtained from first-principles calculations for $CuTlSe_2$ in Ref. [15]. Further simplifications were applied, by neglecting the anisotropic features of the original Hamiltonian, since our sample is in powder form and its anisotropic features would be averaged out. The additional quadratic term alters the energy-momentum dispersion relation and also the density of states (DOS) $\rho(E)$. In the Weyl regime, where the energy scales linearly with k, we expect $\rho(E)$ to scale as $\sim E^2$. However, at high temperatures, the k^2 term in Eq. (3) overwhelms the linear term, leading to a normal metallic regime, where $\rho(E)$ scales as $E^{1/2}$.

The transition between these regimes is illustrated in Fig. 5. We can explain the transition as follows. The NMR spin-relaxation rate is sensitive to the density of states, but, in accordance with the temperature-dependent chemical-potential theory introduced above, its temperature dependence is ultimately determined by a combination of the temperature $k_{\mathrm{B}}T$ and chemical potential $\mu(T)$, the latter decreasing with increasing temperature. Hence, there are two regimes: a low-temperature $k_{\mathrm{B}}T \ll \mu$ regime and a high-temperature $k_{\mathrm{B}}T \gg \mu$ regime. At low temperatures, where $k_{\mathrm{B}}T \ll \mu$ [Fig. 5(a)], the dominant energy scale is the chemical potential, leading to a constant relaxation rate. As the temperature increases, the chemical potential starts to decrease, but it is still the dominant energy scale, so $1/T_1$ also tracks μ and decreases [Fig. 5(b)]. When thermal energy overwhelms the chemical potential, the relaxation rate reaches its minimum and then it starts to grow with temperature [Fig. 5(c)]. Upon further increasing the temperature, we reach a point where the normal metallic states overwhelm the Weyl states and the dispersion changes from linear to quadratic in k. This transition also occurs in the NMR relaxation rate where, at ca. 100 K, the T^2 temperature dependence becomes linear in T [Fig. 5(d)].

Although the above theory explains the different regimes, to understand the observed temperature dependence in detail, we must consider the orbital component of the hyperfine interaction. Such contribution influences primarily the NMR relaxation rate [27,33]. This takes the form

$$\mathscr{H}_{\mathrm{HFI}}^{\mathrm{orb}} = \mathscr{H}_{\mathrm{HFI}}^{\mathrm{lin}} + \mathscr{H}_{\mathrm{HFI}}^{\mathrm{quad}}, \quad \text{where} \tag{4}$$

$$\mathscr{H}_{\mathrm{HFI}}^{\mathrm{lin}} = \frac{\mu_0}{q^2} ie v_{\mathrm{F}} \mathbf{m}(\mathbf{q} \times \boldsymbol{\sigma}), \tag{5}$$

$$\mathscr{H}_{\mathrm{HFI}}^{\mathrm{quad}} = \frac{\mu_0}{q^2} ig\mu_{\mathrm{B}}^*(\mathbf{k}_1 \times \mathbf{k}_2)\sigma_0. \tag{6}$$

Here, μ_0 denotes the vacuum permeability, v_F denotes the Fermi velocity, $\mathbf{m} = \hbar\gamma_{\mathrm{n}}\mathbf{I}$ is the magnetic moment of the nucleus with nuclear gyromagnetic ratio γ_{n} and spin $\mathbf{I}$, $\mu_{\mathrm{B}}^* = \hbar e/(2m^*)$ is the effective Bohr magneton, $g = 2$, $\mathbf{k}_1$ and $\mathbf{k}_2$ are the incoming and outgoing wave vectors, respectively, and $\mathbf{q} = \mathbf{k}_1 - \mathbf{k}_2$. It is worth noting that the expression for the hyperfine interaction in Eq. (4) is already obtained for free electrons in Ref. [34].

For temperatures below T_{onset} (here, 100 K), Eq. (5) is dominant. In this case, the relaxation rate takes the form reported in Refs. [27,33], namely,

$$\frac{\hbar}{k_{\mathrm{B}}T_1T} = \frac{52.7\pi\mu_0^2\gamma_{\mathrm{n}}^2e^2}{(2\pi)^6 v_{\mathrm{F}}^2} \times \begin{cases} \left(\frac{k_{\mathrm{B}}T}{\hbar}\right)^2 \frac{\pi^2}{3} \ln\left(\frac{4k_{\mathrm{B}}T}{\hbar\omega_0}\right), & \mu \ll k_{\mathrm{B}}T, \\ \left(\frac{\mu}{\hbar}\right)^2 \ln\left(\frac{2\mu}{\hbar\omega_0}\right), & \mu \gg k_{\mathrm{B}}T, \end{cases} \tag{7}$$

where k_{B} denotes the Boltzmann constant, ω_0 denotes the nuclear Larmor frequency, and μ denotes the chemical potential.

Likewise, NMR shifts take the form

$$K(\mu, T) \approx \frac{\mu_0 e}{4\pi^2 \hbar}\left[\frac{g\mu_B}{\hbar v_F}\mu - \frac{e v_F}{3}\ln\left(\frac{W}{\max\left[|\mu|, k_B T\right]}\right)\right], \tag{8}$$

where W denotes a constant regularization cutoff. According to Eq. (7), for $T < 30$ K, the relaxation rate is expected to be constant for a fixed μ. However, if $\mu(T)$ is assumed to be temperature dependent, then, as demonstrated in the case of TaP, $\mu(T)$ can be chosen phenomenologically to reproduce the desired $T^{-0.5}$ scaling behavior [27].

In the intermediate temperature region, the temperature starts to increase, with the expected $1/T_1T \sim T^2$ behavior for Weyl semimetals [27,33,35,36] arising from the orbital part of the hyperfine interaction defined in Eq. (5).

In the high-temperature region, we need to consider the quadratic term in Eq. (3). In this case, the Korringa relation connects the relaxation rate and the DOS and is defined as [37]

$$\frac{1}{T_1 T} = \frac{\pi k_B}{\hbar} A_{hf}^2 \rho^2(k_B T), \tag{9}$$

where A_{hf} is the hyperfine coupling. In this regime, $\rho(E) \sim E^{1/2}$, yields the observed linear temperature dependence for the relaxation rate.

When the quadratic term is the dominant one, we can keep only the $\mathscr{H}_{HFI}^{quad}$ term in Eq. (4). Following the same steps as in Ref. [27], we end up with $(T_1T)^{-1} \sim |E| \ln[E/(\hbar\omega)]$, where $E = \max[\mu, k_B T]$, an expression which agrees with the results for ordinary metals [34].

A similar model, with three distinct temperature regimes with different T_1T scalings, was also proposed in a recent theoretical study [38], where the temperature dependence of a disordered Weyl fermion system was postulated to arise from a disorder-induced critical transition (CT). In this case, three regimes were identified: regime I (medium disorder), where the energy dependence of the density of states is dominated by the CT, regime II (low disorder), which corresponds to weakly disordered systems at low energy, and regime III (high disorder), where the density of states becomes nonzero at the Weyl point. Furthermore, the same theoretical study predicts that $(T_1T)^{-1}$ should scale as T^1 in the CT regime, as T^2 in the low disorder regime, and as T^0 in the high disorder regime. Since, in $CuTlSe_2$, the Korringa product T_1TK^2 is constant above T_{onset} and close to the Korringa product of the pure Cu metal, we propose that the origin of the linear temperature dependence of $(T_1T)^{-1}$ is likely due to a simple Fermi-liquid behavior rather than to the more complicated disorder-induced CT regime proposed in Ref. [38]. Nevertheless, the behavior of disordered Weyl-fermion systems remains an interesting open problem, to be addressed by systematic investigations of controllably doped systems.

VII. CONCLUSION

A comprehensive investigation using electronic and magnetic probes confirms that $CuTlSe_2$ is an ideal nonmagnetic Weyl semimetal. Below 100 K, Weyl fermion excitations are evidenced by chiral transport in the magnetoresistance and by the temperature dependence of the nuclear spin-lattice relaxation time T_1. Although macroscopic magnetization measurements show a paramagnetic behavior below 50 K, this is related to minor impurity phases. Indeed, local microscopic probes, such as μSR and NMR, mostly unaffected by tiny magnetic impurities, confirm the ideal Weyl-semimetal behavior to be intrinsic. Further, zero-field μSR results indicate that time-reversal symmetry is preserved in $CuTlSe_2$. Hence, the unusual electronic properties we observe are solely due to the breaking of spatial-inversion symmetry.

On increasing the temperature above 100 K, $CuTlSe_2$ crosses over to a normal-metal regime, reflecting the thermally excited carriers crossing the energy gap of the topologically trivial electronic bands. Such a crossover is observed in the temperature-dependent Hall coefficient suggesting that, above 100 K, the dominant carriers behave as standard electrons. Additionally, above 100 K, a temperature-dependent crossover appears in the muon-spin depolarization rate, implying a change in the muon hyperfine coupling induced by the local electronic density, again consistent with a change in the electronic state. The qualitative description of the corresponding behavior in the NMR relaxation is achieved by means of a two-component effective Hamiltonian.

The results presented here could stimulate interest in similar chalcopyrites, such as $AgTlTe_2$, $AuTlTe_2$, and $ZnPbAs_2$, which likewise might behave as ideal Weyl semimetals.

ACKNOWLEDGMENTS

This work was supported by the Swiss National Science Foundation (Grants No. 200021_188706, No. 200021_-169455, and No. 206021_139082) and, in part, by EPSRC (Grant No. EP/N024028/1). This work was also supported by the National Natural Science Foundation of China (Grant No. 12274440), the Strategic Priority Research Program (B) of Chinese Academy of Sciences (Grant No. XDB33010100), and the Ministry of Science and Technology of China (Grant No. 2022YFA1403903). We acknowledge the allocation of muon beamtime and the beamline support team at SμS and ISIS.

APPENDIX: METHODS AND TECHNIQUES

1. Sample preparation and characterization

Single crystals of $CuTlSe_2$ were grown from Se flux. Stoichiometric amounts of the starting materials Tl_2Se (99.9%), Cu (99.9%), and Se (99.999%), all from Alfa Aesar, were mixed homogeneously and sealed in a quartz tube. The mixture was then melted at 250 °C for 48 h and the obtained ingots were crushed into powders. Polycrystalline $CuTlSe_2$ was sealed in a quartz tube together with an excess of Se powder, heated to 275 °C for 48 h, and slowly cooled down to 225 °C at a rate of 0.2 °C/h. Thereafter, the quartz tube was heated again to 260 °C for 2 h, where the Se flux was separated from the crystals using a centrifuge. The chemical composition and microstructure analysis were performed on a Hitachi model S-4800 field emission scanning electron microscope (SEM). Magnetic measurements were performed using a MPMS-7 T SQUID VSM system.

The obtained single crystals were characterized via x-ray diffraction (XRD) using Mo Kα radiation ($\lambda = 0.71073$ Å).

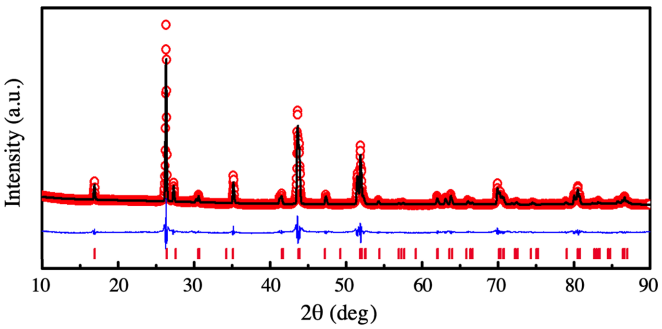

FIG. 6. XRD spectrum of $CuTlSe_2$ obtained at 293 K using Mo Kα radiation.

The XRD spectrum is shown in Fig. 6 and the fitted XRD parameters are provided in Table I. A comparison of the fit values obtained at 100 K and 293 K indicates that the structural parameters are largely temperature-independent.

2. Transport experiments

Magnetic-susceptibility measurements were performed on $CuTlSe_2$ single crystals using a Quantum Design MPMS superconducting quantum interference device (SQUID) magnetometer. Electrical-resistivity measurements were performed on $CuTlSe_2$ single crystals using a Quantum Design physical property measurement system (PPMS). The magnetoresistance was analyzed using the model described in Ref. [21], where C_W denotes the chiral anomaly contribution, C_{WAL} denotes the weak Anderson localization contribution, σ_0 is a field-independent contribution, and B_c is the critical field:

$$\sigma_{xx}(B) = 8C_{\mathrm{W}}B^2 - C_{\mathrm{WAL}}\left(\sqrt{B}\frac{B^2}{B^2+B_c^2} + \gamma B^2\frac{B_c^2}{B^2+B_c^2}\right) + \sigma_0.$$

Since the magnetoresistance of $CuTlSe_2$ is small, here we ignore the off-diagonal components of the magnetoconductivity matrix and assume that the change in magnetoresistance is approximately the opposite of that in magnetoconductivity, i.e., $MR_{xx}(B) - MR_{xx}(0) \approx \sigma_{xx}(0) - \sigma_{xx}(B)$. Hence, the original equation can be rewritten as

$$\Delta MR_{xx}(B) = -8C_{\mathrm{W}}B^2 + C_{\mathrm{WAL}}\left(\sqrt{B}\frac{B^2}{B^2+B_{\mathrm{c}}^2} + \gamma B^2\frac{B_{\mathrm{c}}^2}{B^2+B_c^2}\right).$$

In this model, B_c is the crossover field, which is known to be related to the phase-coherence length l_ϕ by

$$B_c \sim \frac{\hbar}{e\ell_\phi^2}.$$

TABLE I. Crystallographic data and XRD fit parameters for $CuTlSe_2$.

Parameter	Value	
Wavelength	0.71073 Å	
$F(000)$	712	
Crystal system	Tetragonal	
Angles α, β, and γ	$\alpha = 90^\circ$, $\beta = 90^\circ$, $\gamma = 90^\circ$	
Index ranges	$-7 \leqslant h \leqslant 7$, $-7 \leqslant k \leqslant 7$, $-15 \leqslant l \leqslant 15$	
Temperature	293(2) K	100(2) K
Space group	$I\bar{4}2d$ (No. 122)	$I\bar{4}2d$ (No. 122)
Unit-cell parameters	$a = 5.82800(10)$ Å	$a = 5.8216(6)$ Å
	$b = 5.82800(10)$ Å	$b = 5.8216(6)$ Å
	$c = 11.7766(6)$ Å	$c = 11.7413(13)$ Å
Volume	400.00(2) Å^3	397.92(9) Å^3
Density (calculated)	7.071 g/cm^3	7.108 g/cm^3
Absorption coefficient	63.500 mm^{-1}	63.831 mm^{-1}
Theta range	3.90 to 28.40°	3.91 to 28.30°
RMS dev. from mean	0.909 eÅ^{-3}	0.536 e Å^{-3}
Goodness-of-fit on F^2	1.216	1.151
Final R indices (all data)	$R_1 = 0.0339$	$R_1 = 0.0208$
	$wR_2 = 0.0757$	$wR_2 = 0.0448$

3. NMR experiments

The NMR experiments, including lineshape- and spin-lattice relaxation-time measurements, were performed on $CuTlSe_2$ in powder form in an applied magnetic field of 5 and 7 T. The NMR signal was detected by means of a standard spin-echo sequence, consisting of $\pi/2$ and π pulses of 3 and 6 µs, with recycling delays ranging from 1 to 60 s, in the 1.8–300 K temperature range. Despite an echo delay of 100 µs, 2 to 32 scans were sufficient to acquire a good-quality signal. The lineshapes were obtained via fast Fourier transform (FFT) of the echo signal. The spin-lattice relaxation times T_1 were measured via the inversion-recovery method, using a $\pi - \pi/2 - \pi$ pulse sequence.

4. Muon-spin rotation and relaxation (µSR)

The µSR experiments were conducted on the GPS spectrometers of the Swiss muon source (SµS) at Paul Scherrer Institut (PSI) in Villigen, Switzerland, and on the EMU spectrometer at ISIS, Didcot, UK. For the zero-field and weak transverse field µSR measurements, the muon spin was aligned antiparallel to the muon-beam direction. An active stray-field compensation setup was employed to maintain a magnetic field background below 10 µT at the sample position. For the GPS experiments, a polycrystalline sample in pressed pellet form, 10 mm in diameter and 2 mm thick, was suspended in the muon beam using Kapton tape, whereas for the EMU experiments, the same sample was glued on a standard silver plate. For the transverse field µSR experiments, the sample was field cooled and the temperature-dependent data were collected upon warming.

The µSR data were analyzed using the `musrfit` program [39]. The depolarization function $A(t)/A_0 = f_{\mathrm{nm}}e^{-1/2\sigma^2t^2} + (1 - f_{\mathrm{nm}})e^{-\lambda t}$ was used to describe the ZF-µSR data, where A_0 is the initial asymmetry, f_{nm} is the nonmagnetic volume fraction of the sample, σ is the Gaussian relaxation rate of muon spins, while λ is the Lorentzian relaxation rate accounting for the fast initial depolarization. The muon-spin asymmetry in an applied magnetic field takes the form: $A(t)/A_0 = [f_{\mathrm{nm}}e^{-1/2\sigma^2t^2} + f_{\mathrm{bg}}e^{-1/2\sigma_{\mathrm{bg}}^2t^2}]\cos(\omega t + \phi) +$

$(1 - f_{nm} - f_{bg})e^{-\lambda t}$, where f_{bg} represents the muon fraction implanted in the background and $\omega = \gamma_\mu B$. Here, $\gamma_\mu/2\pi = 135.53\,\mathrm{MHz/T}$ is the muon gyromagnetic ratio and B is the strength of the external magnetic field.

5. Determination of the muon-stopping sites

To understand the origin of the contributions to the μSR signal, we carried out density functional theory (DFT) calculations to locate the most probable muon stopping sites [40]. The calculations were carried out using the MuFinder software [41] and the plane-wave-based code CASTEP [42] using the local density approximation. We used supercells consisting of $2 \times 2 \times 1$ unit cells to minimize the effects of muon self-interaction resulting from the periodic boundary conditions. Muons, modeled by an ultrasoft hydrogen pseudopotential, were initialized in range of low-symmetry positions and the structure was allowed to relax (keeping the unit cell fixed) until the change in energy per ion was less than 2×10^{-5} eV. We used a cutoff energy of ≈460 eV and a $1 \times 1 \times 1$ Monkhorst-Pack grid [43] for sampling the k-space.

At each muon site, we computed the expected relaxation rate due to the nuclear dipole moments by using the van Vleck second moment in the limit of strong quadrupolar splitting [44]. In a zero-field experiment this formalism predicts a relaxation rate given by

$$\sigma_{VV}^2 = \frac{4}{9}\sum_i B_i Q(I), \tag{A1}$$

with

$$B_i = \left(\frac{\mu_0}{4\pi}\right)^2 I(I+1)\gamma_\mu^2\gamma_I^2\hbar^2 r_i^{-6}. \tag{A2}$$

Here, the nucleus with spin I and gyromagnetic ratio γ_I is located at site i, at a distance r_i from the muon. The nuclear gyromagnetic ratio is $\gamma_I = g\mu_N/\hbar$, where μ_N is the nuclear magneton, while the g factor is related to the nuclear magnetic moment μ via $g = \mu/I$. For an integer spin I, the factor $Q(I)$ is 1, while for half-integer spins it is given by

$$Q(I) = 1 + \frac{3(I+1/2)}{8I(I+1)}. \tag{A3}$$

The linearity of Eq. (A1) allows us to straightforwardly deal with different isotopes. Consider a nucleus of species i with multiple isotopes α each having nuclear spin I_α, magnetic moment μ_α, and natural abundance f_α. Experimentally, each muon at a crystallographically distinct site would see one of the many possible isotope configurations. However, for an ensemble containing a large number of muons, the linearity of Eq. (A1) makes the summation over all possible configurations very straightforward, yielding the result

$$\sigma_{VV}^2 = \frac{4}{9}\sum_{i,\alpha} f_\alpha B_{i,\alpha} Q(I_\alpha). \tag{A4}$$

[1] B. Yan and C. Felser, Topological materials: Weyl semimetals, Annu. Rev. Condens. Matter Phys. **8**, 337 (2017).

[2] A. A. Burkov and L. Balents, Weyl semimetal in a topological insulator multilayer, Phys. Rev. Lett. **107**, 127205 (2011).

[3] H. Weyl, Elektron und Gravitation. I, Z. Phys. **56**, 330 (1929).

[4] T. Lancaster and S. Blundell, *Quantum Field Theory for the Gifted Amateur* (Oxford University Press, Oxford, UK, 2014).

[5] H. B. Nielsen and M. Ninomiya, The Adler-Bell-Jackiw anomaly and Weyl fermions in a crystal, Phys. Lett. B **130**, 389 (1983).

[6] T. Wehling, A. Black-Schaffer, and A. Balatsky, Dirac materials, Adv. Phys. **63**, 1 (2014).

[7] Y. Xu, L. Elcoro, Z.-D. Song, B. J. Wieder, M. G. Vergniory, N. Regnault, Y. Chen, C. Felser, and B. A. Bernevig, High-throughput calculations of magnetic topological materials, Nature (London) **586**, 702 (2020).

[8] H. Yasuoka, T. Kubo, Y. Kishimoto, D. Kasinathan, M. Schmidt, B. Yan, Y. Zhang, H. Tou, C. Felser, A. P. Mackenzie, and M. Baenitz, Emergent Weyl fermion excitations in TaP explored by ^{181}Ta quadrupole resonance, Phys. Rev. Lett. **118**, 236403 (2017).

[9] C. G. Wang, Y. Honjo, L. X. Zhao, G. F. Chen, K. Matano, R. Zhou, and G. Q. Zheng, Landau diamagnetism and Weyl-fermion excitations in TaAs revealed by ^{75}As NMR and NQR, Phys. Rev. B **101**, 241110(R) (2020).

[10] D. Hsieh, Y. Xia, L. Wray, D. Qian, A. Pal, J. H. Dil, J. Osterwalder, F. Meier, G. Bihlmayer, C. L. Kane, Y. S. Hor, R. J. Cava, and M. Z. Hasan, Observation of unconventional quantum spin textures in topological insulators, Science **323**, 919 (2009).

[11] T. Yokoo, Y. Watanabe, M. Kumazaki, M. Itoh, and Y. Shimizu, Site-dependent local spin susceptibility and low-energy excitation in a Weyl semimetal WTe_2, J. Phys. Soc. Jpn. **91**, 054701 (2022).

[12] L. X. Zheng, K. F. Luo, Z. L. Sun, D. Zhao, J. Li, D. W. Song, S. J. Li, B. L. Kang, L. P. Nie, M. Shan, Z. M. Wu, Y. B. Zhou, X. Dai, H. M. Weng, R. Yu, T. Wu, and X. H. Chen, Magnetic-field-induced electronic instability of Weyl-like fermions in compressed black phosphorus, Sci. China: Phys. Mech. Astron. **66**, 117011 (2023).

[13] M. G. Vergniory, L. Elcoro, C. Felser, N. Regnault, B. A. Bernevig, and Z. Wang, A complete catalogue of high-quality topological materials, Nature (London) **566**, 480 (2019).

[14] M. M. Otrokov, I. I. Klimovskikh, H. Bentmann, D. Estyunin, A. Zeugner, Z. S. Aliev, S. Gaß, A. U. B. Wolter, A. V. Koroleva, A. M. Shikin, M. Blanco-Rey, M. Hoffmann, I. P. Rusinov, A. Y. Vyazovskaya, S. V. Eremeev, Y. M. Koroteev, V. M. Kuznetsov, F. Freyse, J. Sánchez-Barriga, I. R. Amiraslanov *et al.*, Prediction and observation of an antiferromagnetic topological insulator, Nature (London) **576**, 416 (2019).

[15] J. Ruan, S.-K. Jian, D. Zhang, H. Yao, H. Zhang, S.-C. Zhang, and D. Xing, Ideal Weyl semimetals in the chalcopyrites $CuTlSe_2$, $AgTlTe_2$, $AuTlTe_2$, and $ZnPbAs_2$, Phys. Rev. Lett. **116**, 226801 (2016).

[16] J. S. Bell and R. Jackiw, A PCAC puzzle: $\pi^0 \to \gamma\gamma$ in the σ-model, Nuovo Cimento A **60**, 47 (1969).

[17] N. P. Armitage, E. J. Mele, and A. Vishwanath, Weyl and Dirac semimetals in three-dimensional solids, Rev. Mod. Phys. **90**, 015001 (2018).

[18] S. A. Parameswaran, T. Grover, D. A. Abanin, D. A. Pesin, and A. Vishwanath, Probing the chiral anomaly with nonlocal transport in three-dimensional topological semimetals, Phys. Rev. X **4**, 031035 (2014).

[19] A. A. Burkov, Chiral anomaly and diffusive magnetotransport in Weyl metals, Phys. Rev. Lett. **113**, 247203 (2014).

[20] X. Huang, L. Zhao, Y. Long, P. Wang, D. Chen, Z. Yang, H. Liang, M. Xue, H. Weng, Z. Fang, X. Dai, and G. Chen, Observation of the chiral-anomaly-induced negative magnetoresistance in 3D Weyl semimetal TaAs, Phys. Rev. X **5**, 031023 (2015).

[21] C.-L. Zhang, S.-Y. Xu, I. Belopolski, Z. Yuan, Z. Lin, B. Tong, G. Bian, N. Alidoust, C.-C. Lee, S.-M. Huang, T.-R. Chang, G. Chang, C.-H. Hsu, H.-T. Jeng, M. Neupane, D. S. Sanchez, H. Zheng, J. Wang, H. Lin, C. Zhang *et al.*, Signatures of the Adler–Bell–Jackiw chiral anomaly in a Weyl fermion semimetal, Nat. Commun. **7**, 10735 (2016).

[22] J. Du, H. Wang, Q. Chen, Q. Mao, R. Khan, B. Xu, Y. Zhou, Y. Zhang, J. Yang, B. Chen, C. Feng, and M. Fang, Large unsaturated positive and negative magnetoresistance in Weyl semimetal TaP, Sci. China: Phys. Mech. Astron. **59**, 657406 (2016).

[23] A. C. Niemann, J. Gooth, S.-C. Wu, S. Bäßler, P. Sergelius, R. Hühne, B. Rellinghaus, C. Shekhar, V. Süß, M. Schmidt, C. Felser, B. Yan, and K. Nielsch, Chiral magnetoresistance in the Weyl semimetal NbP, Sci. Rep. **7**, 43394 (2017).

[24] C. Shekhar, A. K. Nayak, Y. Sun, M. Schmidt, M. Nicklas, I. Leermakers, U. Zeitler, Y. Skourski, J. Wosnitza, Z. Liu, Y. Chen, W. Schnelle, H. Borrmann, Y. Grin, C. Felser, and B. Yan, Extremely large magnetoresistance and ultrahigh mobility in the topological Weyl semimetal candidate NbP, Nat. Phys. **11**, 645 (2015).

[25] T. Andrearczyk, J. Jaroszyński, G. Grabecki, T. Dietl, T. Fukumura, and M. Kawasaki, Spin-related magnetoresistance of *n*-type ZnO:Al and $Zn_{1-x}Mn_xO$: Al thin films, Phys. Rev. B **72**, 121309(R) (2005).

[26] M. Koshino and I. F. Hizbullah, Magnetic susceptibility in three-dimensional nodal semimetals, Phys. Rev. B **93**, 045201 (2016).

[27] Z. Okvátovity, H. Yasuoka, M. Baenitz, F. Simon, and B. Dóra, Nuclear spin-lattice relaxation time in TaP and the Knight shift of Weyl semimetals, Phys. Rev. B **99**, 115107 (2019).

[28] S. J. Blundell, R. De Renzi, T. Lancaster, and F. L. Pratt, *Muon Spectroscopy: An Introduction* (Oxford University Press, Oxford, UK, 2022).

[29] A. D. Huxley, P. Dalmas de Reotier, A. Yaouanc, D. Caplan, M. Couach, P. Lejay, P. C. M. Gubbens, and A. M. Mulders, $CeRu_2$: A magnetic superconductor with extremely small magnetic moments, Phys. Rev. B **54**, R9666 (1996).

[30] A. T. Fiory, A review of studies of magnetism and magnetic materials by means of the μSR technique, Hyperfine Interact. **6**, 63 (1979).

[31] V. G. Storchak and N. V. Prokof'ev, Quantum diffusion of muons and muonium atoms in solids, Rev. Mod. Phys. **70**, 929 (1998).

[32] D. G. C. Jonas, P. K. Biswas, A. D. Hillier, D. A. Mayoh, and M. R. Lees, Quantum muon diffusion and the preservation of time-reversal symmetry in the superconducting state of type-I rhenium, Phys. Rev. B **105**, L020503 (2022).

[33] Z. Okvátovity, F. Simon, and B. Dóra, Anomalous hyperfine coupling and nuclear magnetic relaxation in Weyl semimetals, Phys. Rev. B **94**, 245141 (2016).

[34] A. Knigavko, B. Mitrović, and K. V. Samokhin, Divergence of the orbital nuclear magnetic relaxation rate in metals, Phys. Rev. B **75**, 134506 (2007).

[35] H. Maebashi, T. Hirosawa, M. Ogata, and H. Fukuyama, Nuclear magnetic relaxation and Knight shift due to orbital interaction in Dirac electron systems, J. Phys. Chem. Solids **128**, 138 (2019).

[36] T. Hirosawa, H. Maebashi, and M. Ogata, Nuclear spin relaxation time due to the orbital currents in Dirac electron systems, J. Phys. Soc. Jpn. **86**, 063705 (2017).

[37] H. Alloul, NMR studies of electronic properties of solids, Scholarpedia **9**, 32069 (2014).

[38] T. Hirosawa, H. Maebashi, and M. Ogata, Nuclear spin relaxation rate near the disorder-driven quantum critical point in Weyl fermion systems, Phys. Rev. B **101**, 155103 (2020).

[39] A. Suter and B. M. Wojek, Musrfit: A free platform-independent framework for μSR data analysis, Phys. Procedia **30**, 69 (2012).

[40] J. S. Möller, P. Bonfà, D. Ceresoli, F. Bernardini, S. J. Blundell, T. Lancaster, R. D. Renzi, N. Marzari, I. Watanabe, S. Sulaiman, and M. I. Mohamed-Ibrahim, Playing quantum hide-and-seek with the muon: Localizing muon stopping sites, Phys. Scr. **88**, 068510 (2013).

[41] B. M. Huddart, A. Hernández-Melián, T. J. Hicken, M. Gomilšek, Z. Hawkhead, S. J. Clark, F. L. Pratt, and T. Lancaster, MuFinder: A program to determine and analyse muon stopping sites, Comput. Phys. Commun. **280**, 108488 (2022).

[42] M. D. Segall, P. J. D. Lindan, M. J. Probert, C. J. Pickard, P. J. Hasnip, S. J. Clark, and M. C. Payne, First-principles simulation: Ideas, illustrations, and the CASTEP code, J. Phys.: Condens. Matter **14**, 2717 (2002).

[43] H. J. Monkhorst and J. D. Pack, Special points for Brillouin-zone integrations, Phys. Rev. B **13**, 5188 (1976).

[44] R. S. Hayano, Y. J. Uemura, J. Imazato, N. Nishida, T. Yamazaki, and R. Kubo, Zero-and low-field spin relaxation studied by positive muons, Phys. Rev. B **20**, 850 (1979).